Alternative method of making electrical connections in the 1st and 3rd generation modules as an effective way to improve module efficiency and reduce production costs

PAWEŁ KWAŚNICKI[a, b]
ANNA GRONBA-CHYŁA[a*]
AGNIESZKA GENEROWICZ[c]
JÓZEF CIUŁA[d]
IWONA WIEWIÓRSKA[e]
KRZYSZTOF GASKA[f]

[a] John Paul II Catholic University of Lublin, Faculty of Natural and Technical Sciences, Konstantynów 1 H, 20-708 Lublin, Poland

[b] Research & Development Centre for Photovoltaics, ML System S.A., Zaczernie 190G, 36-062 Zaczernie, Poland

[c] Cracow University of Technology, Department of Environmental Technologies, Warszawska 24, 31-155 Cracow, Poland

[d] State University of Applied Sciences in Nowy Sącz, Faculty of Engineering Sciences, Zamenhofa 1A, 33-300 Nowy Sącz, Poland

[e] Sądeckie Wodociągi sp. z o.o., W. Pola 22, 33-300 Nowy Sącz, Poland

[f] Silesian University of Technology, Faculty of Energy and Environmental Engineering, Konarskiego 18, 44-100 Gliwice, Poland

Abstract   In this work, we propose a new method for manufacturing busbars in photovoltaic modules for different solar cell generations, focusing on 1st and 3rd generations. The method is based on high-pressure spray coating using nanometric metallic powder. Our focus is primarily on optimizing conductive paths for applications involving conductive layers used in 3rd generation solar cells, such as quantum dot solar cell, dye-sensitized solar cell, and silicon-based solar cells on glass-glass architecture for building-

*Corresponding Author. Email: amgronba@kul.pl

integrated photovoltaic. The advantages of the proposed method include the possibility of reducing the material quantity in the conductive paths and creating various shapes on the surface, including bent substrates.

This paper examines the influence of the proposed high-pressure spraying technique using metallic particles on the morphology of the resulting conductive paths, interface characteristics, and electrical parameters. Conductive paths were created on four different layers commonly used in photovoltaic systems, including transparent conductive oxide, Cu, Ti, and atomic layer deposition processed Al_2O_3. The use of high-pressure technology enables the production of conductive layers with strong adhesion to the substrate and precise control of the spatial parameters of conductive paths. Furthermore, the temperature recorded during the deposition process does not exceed 385 K, making this technique suitable for various types of substrates, including glass and silicon. Additionally, the produced layers exhibit low resistance, measuring less than 0.3 Ω. Finally, the mechanical resistance, as determined through tearing tests, as well as environmental and time stability, have been confirmed for the produced paths.

Keywords: Photovoltaics; Busbars; DSSC; BIPV; Solar module

Acronyms

ALD	–	atomic layer deposition
BB	–	busbar
BIPV	–	building integrated photovoltaic
DSSC	–	dye-sensitized solar cell
EDX	–	energy dispersive X-ray spectroscopy
FTO	–	fluorine-doped tin oxide
GG	–	glass-glass
IEC	–	International Electrotechnical Commission
I(U)	–	current-voltage characteristic
PV	–	photovoltaic
PVD	–	physical vapor deposition
SEM	–	scanning electron microscopy
TCO	–	transparent conductive oxide
QDSC	–	quantum dot solar cell

1   Introduction

Photovoltaic (PV) modules possess several crucial parameters that determine their performance and suitability for specific applications. The reliability and lifespan of photovoltaic modules predominantly hinge on degradation and failure modes. Therefore, comprehending the degradation mech-

anisms, including the origins of these degradation modes and their impact on PV module efficiency [1], is an essential and foundational task to enhance the reliability of PV modules [2,3].

One vital parameter relates to busbars and their stability, particularly concerning DSSC (dye-sensitized solar cell) and glass-glass modules. The issue at hand is closely linked to busbar production technology and can be refined through the technological solution proposed in this study. When subjected to cyclic bending, cracks can emerge near the points where the busbars are soldered to the silicon, potentially propagating due to fatigue [4, 5]. Conversely, under cyclic axial strain, the busbars endure loads beyond the elastic limit, leading to plasticity and hysteric energy dissipation [6,7]. Kaule *et al.* demonstrated that the strength and cracking susceptibility are highly dependent on the side and direction of the load, with the lowest strength observed on the rear side loaded with tensile stress parallel to the busbars [8].

Improving module efficiency and reducing production costs are two critical objectives for the photovoltaic industry. Achieving these goals can help make solar energy more competitive with traditional energy sources and enable wider adoption of renewable energy [9–11].

In this paper, we will discuss one of the strategies that can be used to enhance module efficiency and reduce production costs by employing alternative methods for busbar production. Busbars (BBs) are essential components of photovoltaic modules [12, 13] commonly used to generate electricity from solar energy. The primary purpose of busbars in PV modules is to enhance the electrical performance of the module by reducing resistive losses and improving the overall efficiency [14, 15].

In a typical PV module, each solar cell generates a relatively small amount of electricity. Busbars serve to interconnect the cells, increasing the total voltage and current produced by the module. This is necessary because the voltage and current produced by a single solar cell are generally too low to be practical on their own. When solar cells are connected in series to form a module, the cumulative current flowing through each cell adds up, and any resistance in the circuit can result in power losses [16,17]. New techniques involving copper busbars offer the most efficient placement and a simplified amount of materials for PV panels [18, 19]. In fact, the busbar system replaces two crucial components in a typical PV panel: the power distribution block and the connecting cables [20, 21]]. Lu *et al.* observed that optimizing busbars based on the uneven distribution of illumination created by the concentrator contributes to the enhancement of the electrical

parameters of the compound parabolic contractor-photovoltaic (CPC-PV) cell [22–24]. The study of the electromagnetic field distribution due to the incident photon flux demonstrates that increasing the number of busbars can generate carriers in the shaded areas under the busbars [25–27]. Several attempts have been made to reduce material costs in the production of BBs, including the application of shingled technology [28]. Shingled photovoltaic modules involve the process of creating shingled strings by splitting and gluing solar cells [29]. As an adhesive method, the application of divided cell strips across the width of the busbar is used to connect them together using electroconductive adhesive (ECA) [30]. Given the high cost of Ag paste used in the production of solar cells, efforts have been made to reduce its usage as a solar cell electrode. Oh *et al.* employed an economically effective electrode pattern that significantly reduced the amount of Ag paste used [31, 32].

In dye-sensitized solar cells (DSSCs) [33, 34], busbars are employed to connect the individual cells and create an electrical circuit. The photoactive layer consists of a semiconductor material coated with a layer of dye molecules. When light strikes the dye molecules, they absorb the energy and transfer it to the semiconductor, generating an electrical current. Given that the current generated by a DSSC is relatively low, busbars in DSSCs are typically crafted from transparent conductive materials [35], such as Indium Tin Oxide (ITO) or Fluorine-doped Tin Oxide (FTO) [36, 37], and are also used in the form of metallic paths on the edges [38]. These materials provide low-resistance paths for the current to flow through, minimizing resistive losses, and enhancing the electrical performance of the cell.

Glass-glass (GG) [39, 40]] solar cells comprise two glass layers that sandwich the photovoltaic cells, typically silicon-based [41, 42]. The glass layers offer mechanical support and protection for the cells while allowing light to penetrate and reach the cells [43, 44]. Busbars are employed to collect the current generated by the individual cells and transfer it to an external load [45–47]. They also aid in distributing the current evenly across the cell, reducing hot spots and the risk of cell damage. Since GG solar cells are relatively thin [48], the busbars used in these cells are generally composed of highly conductive metals, such as copper or silver [49, 50]. These materials offer low-resistance paths for the current to flow through, minimizing resistive losses and improving the electrical performance of the cell [51, 52]. Additionally, in GG solar cells, busbars can be placed on both sides of the cells, further enhancing current collection and reducing power losses [53].

Reducing the manufacturing cost of busbars is a critical parameter, and considerable efforts have been made in this regard. Cost reduction can be achieved through various means, including:

- Thinning the busbars: Busbars can be made thinner while maintaining their electrical conductivity, thus reducing the required material per busbar.

- Using alternative materials: Instead of copper, which is commonly used for busbars, alternative materials such as aluminum or silver can be employed. These materials offer higher conductivity per unit weight than copper, allowing for a reduction in material usage.

- Utilizing busbarless cell interconnection: In this method, solar cells are interconnected without the need for busbars, eliminating the necessity for busbars entirely.

- Optimizing busbar layout: By carefully designing the layout of the busbars, it is possible to reduce the material requirements for each busbar while maintaining the necessary electrical conductivity.

All of these approaches can be achieved or improved through the high-pressure spraying process described in this paper.

2   Experimental procedure

The busbar paths under investigation have been analysed by means of contact profilometry (DektakX, Bruker) to obtain the cross-sectional shape and thickness of the busbar structures. Additionally, the elemental composition of the alloy was determined using eenergy-dispersive X-ray spectroscopy (EDX), and the interface between the metallic tracks and the substrate was imaged using high-resolution scanning electron microscopy (HR-SEM). Electrical measurements were conducted during the tests using a four-point probe (4-Probe, Ossila BV), an ohmmeter (Keihley), and an emission spectrometer with a glow discharge excitation source (GDS, GD-Profiler 2, Horiba).

Samples of metallic busbars made using the high-pressure spraying method on various types of glass substrates were tested. The substrates were TCO glass in the 1000 mm × 2000 mm format, covered with various nano-coatings. Two of them were created using the physical vapor deposition

(PVD) method (Kenosistec PVD system), containing coatings made of pure copper (Cu) and titanium (Ti). Aluminum (III) oxide (Al_2O_3) was deposited on glass panes using the atomic layer deposition (ALD) technique (Beneq). Additionally, one series of metallic traces was made on uncoated TCO (transparent conductive oxide) glass. The electrodes were spray-coated using a system manufactured by Ceri-com companies, following these parameters: sputtering rate between 30–40 mm/s, busbar width of 5 mm, and the process was conducted at room temperature and standard humidity.

Table 1 summarizes the information on the tested metallic tracks, including sample designations, types of coating, methods of coating deposition, and detailed descriptions of the process.

Table 1: Summary of information on tested metallic tracks.

Designation	Layer	Deposit method	Detailed description of the process
TCO-clear	No layer	–	unmodified TCO glass
TCO-Cu_a	Copper	PVD	2.4 kW, 3 number of rounds, $v = 4$ mm/s
TCO-Cu_b	Copper	PVD	1.4 kW, 3 number of rounds, $v = 4$ mm/s
TCO-Ti_a	Titanium	PVD	2.4 kW, 3 number of rounds, $v = 4$ mm/s
TCO-Ti_b	Titanium	PVD	1.4 kW, 3 number of rounds, $v = 4$ mm/s

v – speed of the substrate during deposition process.

3   Results

3.1   Determination of busbar thickness

The thickness of busbars plays a crucial role in determining the electrical performance of the module. Thicker busbars can offer lower resistance and improved current collection, leading to higher efficiency. However, thicker busbars can also increase shading effects on the cells, potentially reducing the overall power output of the module.

Samples were extracted from both the edge and the center of the glass pane. Each obtained sample, measuring approximately 50 mm × 50 mm, underwent analysis using the methods described above. Figure 1 illustrates the locations where glass fragments with electrodes were collected, exemplified by TCO-Cu_a, which features TCO glass covered with a thin copper (Cu) layer.
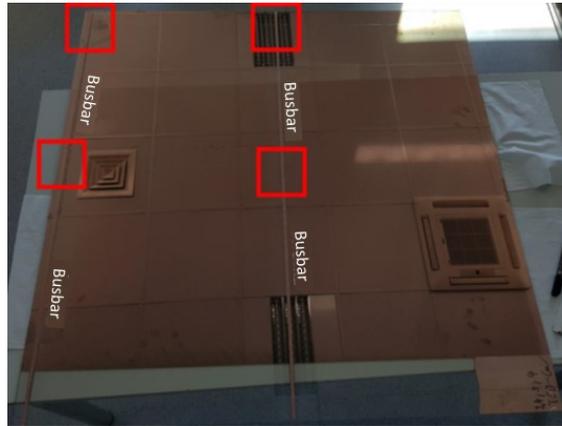
Figure 1: Photograph of TCO-Cu_a glass with marked (red) sampling points for testing.

Needle profilometry was employed to perform scans of the busbar profiles. The scans were conducted across the electrodes, resulting in the left and right sides of the scan containing the substrate profile. This allowed for the measurement of the track's height relative to the substrate. Figure 2 displays several exemplary profiles. While there is a notable difference in their heights relative to each other, the shape of each resembles a Gaussian distribution, albeit not perfectly symmetrical about the center. Due to the significant roughness of the electrodes, thickness measurements were conducted by measuring the relative height between the substrate and the one-
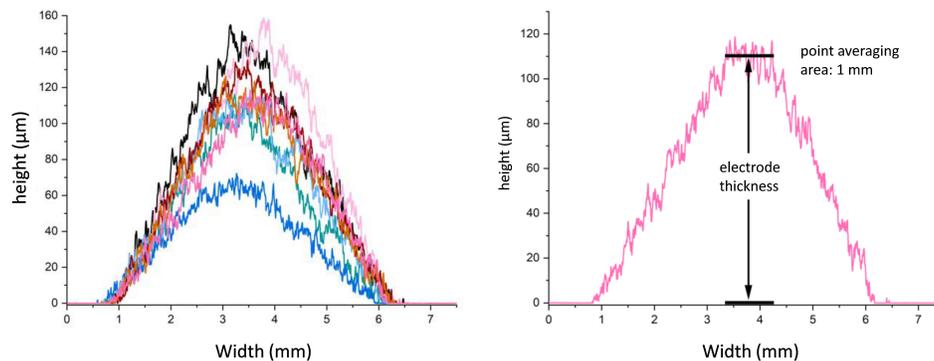
Figure 2: List of several exemplary profiles of the cross-section of metallic tracks, illustrating the method of measuring the thickness of the electrodes (averaging the height from 1 mm of the top of the profile).

millimeter average height of the top of the electrode (as depicted in Fig. 2). The width of each path fluctuated around 5 mm. The average thickness of all collected substrates was 125 ± 16 μm. However, when comparing the smallest (65 μm) and the largest (154 μm) values, it is evident that there is a significant spread.

Lower values predominantly appeared on the edge side, likely where the deposition of tracks commenced. Subsequently, the thickness stabilized, with a few exceptions. Analyzing the thicknesses for individual substrates (Fig. 3), it is apparent that these values closely align with the value determined for all samples, averaging around 125 μm and sharing similar uncertainty values. The largest deviation from the average occurred in the case of the TCO-Ti_a sample, where the average value was 113 ± 7 μm. All thickness values, along with their associated uncertainties, are presented in Table 2. The standard busbar thickness can vary depending on the specific
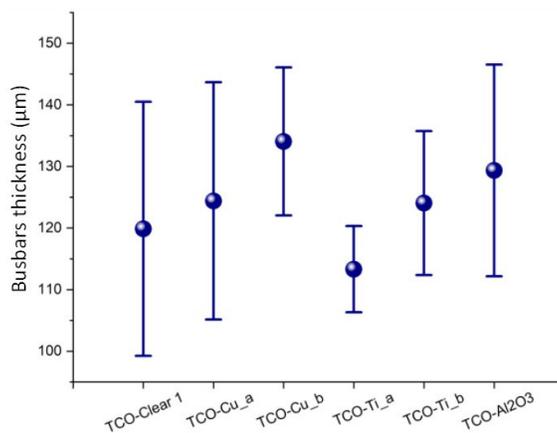
Figure 3: Determined on the basis of collected profiles of constant thickness for all substrates.

Table 2: Average thicknesses determined based on collected profiles for all substrates.

Designation	Busbar thickness (μm)
TCO-Clear	120 ± 21
TCO-Cu_a	124 ± 19
TCO-Cu_b	134 ± 12
TCO-Ti_a	113 ± 7
TCO-Ti_b	124 ± 12

module design and requirements. In general, the thickness of busbars in PV modules can range from 0.1 to 0.5 mm.

3.2   Thermal distribution during the deposition process

The deposition process took place in a room environment with a temperature of 295 K and a maximum humidity of 63%. Temperature measurements at the very surface of the contact point between the beam and the substrate were conducted using a standard pyrometer (laser pyrometer TP10) with a spot size of 1 mm and an accuracy range of ± 1 K. Measurements were performed at three different points on the sample, covering the right, center, and left sides during the deposition process. Once the process pressure stabilized, no significant temperature discrepancies were observed. The measured temperature at 7.2 ± 1 bar pressure was 377.4 ± 2 K.

A slight correlation between temperature and busbar thickness is discernible as shown in Fig. 4. Thicker busbars tend to be associated with higher temperatures. However, it is essential to note that these values fall within the measurement error range. Drawing definitive conclusions from this observed relationship necessitates further testing.
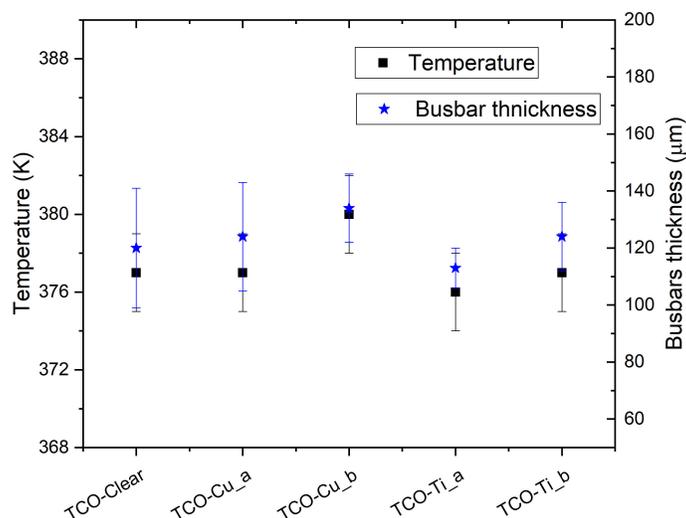
Figure 4: Temperature values for all substrates combined with the busbar thickness.

3.3   Mechanical tear and shear tests

Mechanical tear and shear tests are critical evaluations for assessing the strength and durability of busbars used in various applications, including photovoltaic modules. The tear test involves subjecting busbars to controlled tensile loads until they break or tear. Several standards outline tear test procedures for busbars in PV modules, with reference to the International Electrotechnical Commission (IEC) standard IEC 61215, which specifies requirements for the design and testing of crystalline silicon PV modules. According to IEC 61215, PV module busbars should withstand a minimum tensile force of $30 \, \text{N/mm}^2$ without tearing. This test is typically performed on a module sample containing busbars, applying gradual load until busbar breakage occurs. The tear test serves as a crucial quality control measure to ensure the reliability and durability of busbars in PV modules. By subjecting busbars to controlled tensile loads, the test helps detect potential weaknesses or defects, enabling corrective action before deployment in the field.

Busbar shear tests assess the busbar's ability to endure mechanical stresses and loads typical of its intended application. In PV modules, busbars face various stresses, including thermal expansion, wind loads, and mechanical vibration. These stresses can lead to busbar deformation, cracking, or failure over time, resulting in reduced module efficiency or module failure. The International Electrotechnical Commission standard 61215 for terrestrial PV modules specifies a minimum requirement of 50 N for busbar shear tests. Similarly, the IEC 61646 standard for thin-film PV modules prescribes a minimum requirement of 60 N for the busbar shear test. Nonetheless, these values represent minimum requirements, and manufacturers may opt to exceed them to ensure their modules' mechanical strength and durability.

After conducting a series of measurements on each sample, the average values, regardless of the layer, were found to be $500 \, \text{N/cm}^2$ for the tear test and $600 \, \text{N/m}^2$ for the shear test as presented in Fig. 5. These values significantly exceed those typical for busbars made by conventional methods.
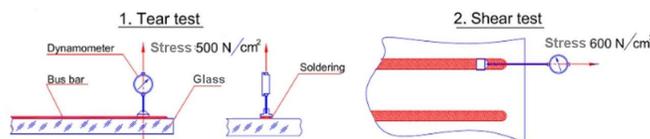

Figure 5: Schematic representation of tear and shear tests.

3.4   SEM imaging

The morphology of the tested samples was analyzed using scanning electron microscopy (SEM). Images were obtained for both the surface of the metallic tracks and the cross-section, which was achieved by cutting and fracturing the glass. Figure 6a presents an image illustrating the boundary between the metallic path (left) and the substrate (right). Upon closer examination in Fig. 6b, it becomes apparent that CuZn alloy particles are present at the boundary regions, although they do not have physical contact with the track. The electrode itself consists of fused particles, forming a highly rugged structure, as depicted in Fig. 6c. This roughness is further emphasized in images 6d to 6f. When observing the material at the nanoscale (Figs. 6g and 6h), nanoroughness becomes apparent, which may, but not necessarily, result from surface oxidation of the track. These nanoscale images reveal both darker and lighter areas, possibly indicating an inhomogeneous distribution of elements within the CuZn alloy or the presence of admixtures (estimated at < 0.5 wt%).

Figure 7a offers a general view of the cross-section of the TCO-clear sample, with a more detailed view in Fig. 7b. Figure 7c displays the interface between the glass, the FTO coating, and the metallic track, indicating a strong connection between these components. It is likely that the glass manufacturer employs an additional, very thin buffer layer of unknown chemical composition (probably SiO_2) between the glass and the FTO coating to prevent ion migration from the glass to the FTO. An inadvertently detached metallic track from the substrate (Fig. 7d) reveals that the detached surface mirrors the rough topography of the FTO coating, implying that during the initial phase of metallic track deposition, the layer is likely liquid or semi-liquid, allowing it to conform to the substrate's surface shape. Upon analyzing the interior of the cross-section (Fig. 7e), it becomes evident that the interior of the metallic path is denser (solid) compared to its surface (as seen in Fig. 6).

Similar conclusions can be drawn for samples with copper (Fig. 8) and titanium (Fig. 9) coatings. The visible cross-sections resemble Gaussian distributions. Metallic tracks exhibit strong adherence to the TCO substrate with the applied coating. During attempts to image the interface between the track and the substrate, it was challenging to directly visualize the metallic coating located between the FTO and the track (Figs. 8c and 9c). These tests were conducted on thinner (TCO-Cu_b, TCO-Ti_b) and thicker metal coatings (TCO-Cu_a, TCO-Ti_a). A slightly brighter
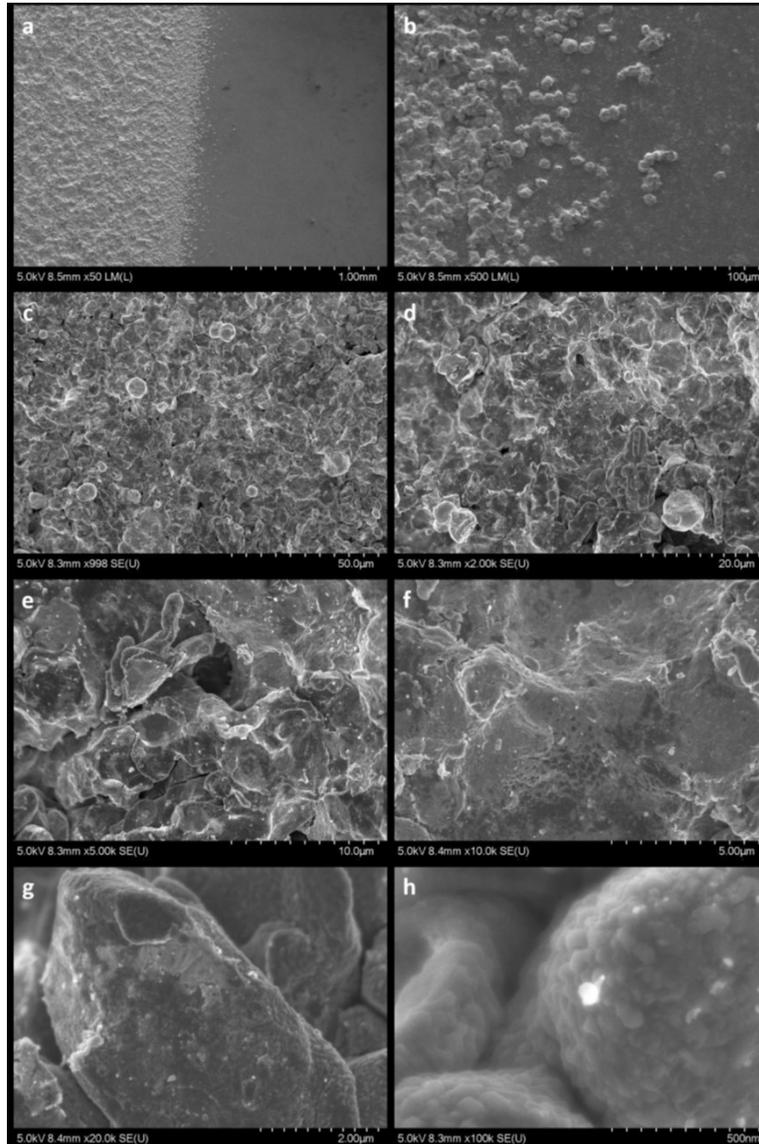
Figure 6: SEM images of the path-substrate boundary (a-b) and of the CuZn alloy surface (c-h) at different magnifications.

appearance in these areas may indicate the presence of a metallic coating, as the cross-section for secondary electron removal is correlated with the atomic number and material density.
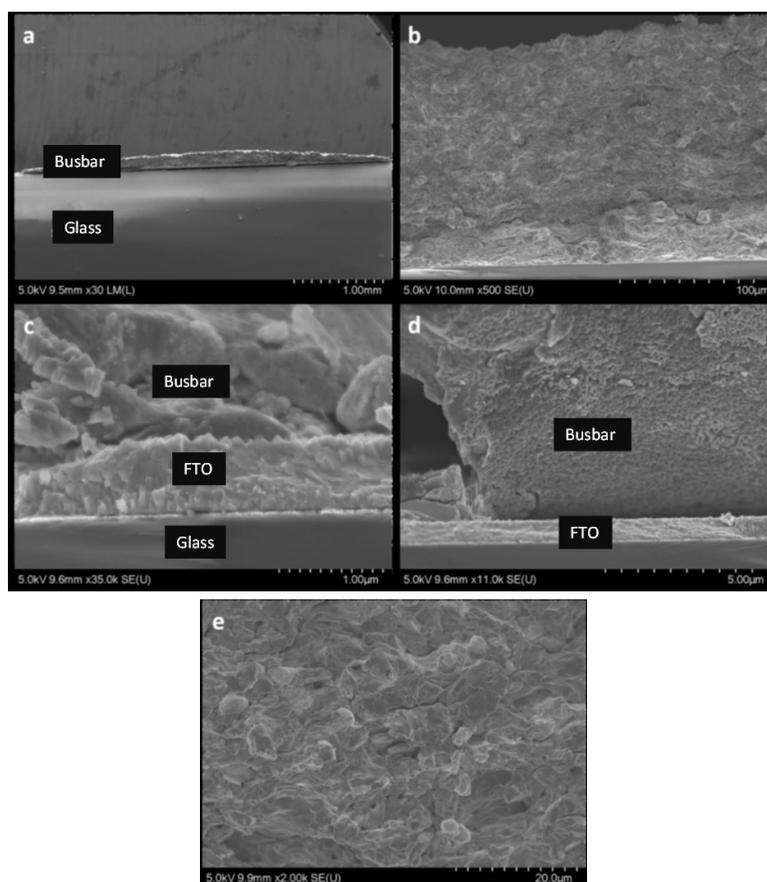
Figure 7: SEM images of the metallic path in the case of the TCO-clear sample: (a)–(b) the general cross-section, (c) the cross-section of the track-substrate interface, (d) the electrode detached from the substrate, (e) the inside of the cross-section.

The interface between the glass, FTO, Al2O3, and the metallic path was also examined for the TCO-Al$_2$O$_3$ sample (Fig. 10c). In this instance, a thin layer of aluminium (III) oxide is prominently visible, appearing notably darker than the surrounding areas, and it uniformly covers the surface of the FTO along its entire length. The larger area of charge accumulation observed on the glass surface (Fig. 10a) suggests that the flow of electrons from the glass to the FTO may be hindered due to the insulating properties of Al$_2$O$_3$. While the charging effect (bright, floating image) was observed for the other samples as well, it was particularly pronounced in this case.
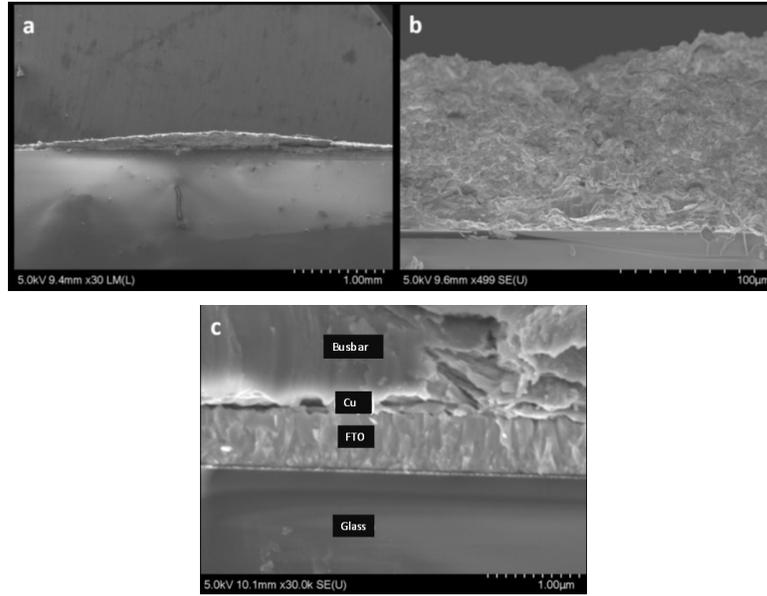
Figure 8: SEM images (a)–(b) showing the general section and (c) the path-substrate interface section obtained for the TCO-Cu_a sample.
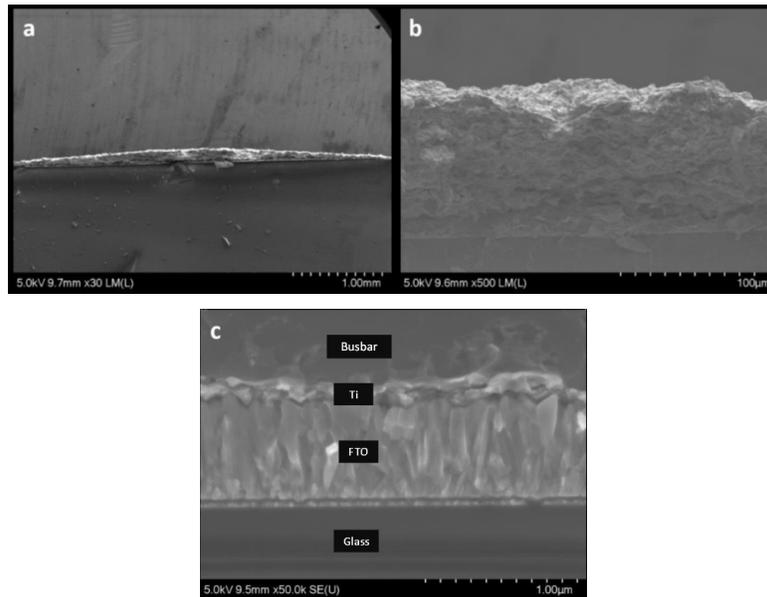
Figure 9: SEM images (a)–(b) displaying the general cross-section and (c) the cross-section of the path-substrate interface for the TCO-Ti_a sample.
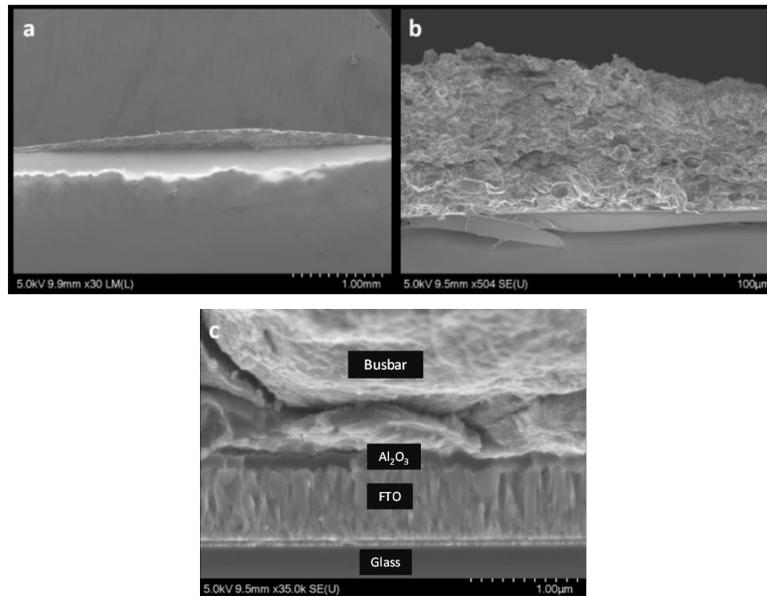
Figure 10: SEM images (a)–(b) of the general section and (c) of the path-substrate interface section obtained for the TCO-Al$_2$O$_3$ sample.

3.5 Energy-dispersive X-ray spectroscopy analysis

The elemental composition of the electrodes was analyzed using EDX spectroscopy. Figure 11 presents an example of a spectrum collected from a me-
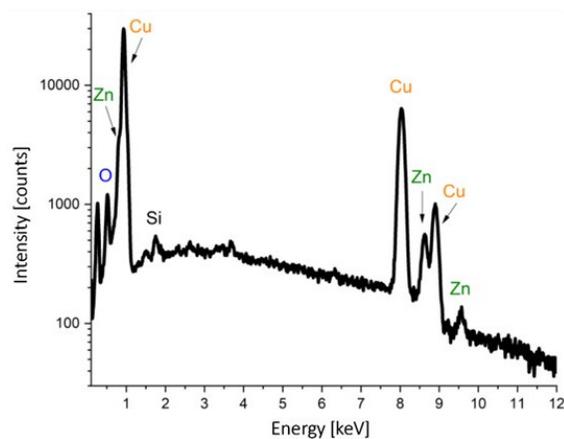
Figure 11: An example spectrum collected in the area of the metallic path from the area of 50 μm × 50 μm.

tallic track deposited on a TCO-clear sample. The spectrum displays characteristic peaks for copper (Cu) and zinc (Zn) atoms. Furthermore, signals from silicon (Si) and oxygen (O) are also present. While the presence of oxygen can be attributed to the oxidation of the metallic track's surface, the silicon content may result from the signal originating from the substrate (FTO glass) or a minor admixture of this element to the CuZn alloy. The former theory appears to be more plausible because, within the energy range of 3–4 keV, small peaks emerge from the noise, typical of tin (Sn) originating from the FTO (SnO_2:F) coating on the glass.

The weight percentage of the elemental composition is presented in Table 3. Upon analysis of the data, it is evident that the metallic traces primarily consist of copper with a notable admixture of zinc. The weight ratio of copper to zinc (Cu/Zn) varies and falls within the range of 2.33 to 3.37.

Table 3: Summary of the percentage by weight elemental compositions for individual samples of metallic paths determined from the collected EDX spectra.

Designation	% by weight				Ratio Cu/Zn
	C	O	Cu	Zn	
TCO-clear	8.1	2.7	68.7	20.4	3.37
TCO-Cu_a	5.6	2.1	68.7	23.7	2.90
TCO-Cu_b	4.7	1.8	71.1	22.4	3.17
TCO-Ti_a	6.8	1.9	70.0	21.3	3.29
TCO-Ti_b	4.9	1.9	70.6	22.6	3.12
TCO-Al2O3	5.0	2.1	64.5	27.7	2.33

3.6 Electrical measurements

The resistance of the busbar is an important electrical parameter that affects the overall efficiency of the module. Lower resistance leads to lower power losses due to Joule heating and results in higher module efficiency. Attempts to measure the electrical properties were made on a device for determining the surface resistance with four probes and a Keithley multimeter. In both cases, the results were unclear and difficult to interpret.

A measurement made with a multimeter showed a resistance of around 0.3 Ω. However, this value is lower than the resistance on the measuring probes, because when shorting them together, the device showed a resistance of about 0.4 Ω. This value indicates the resistance of the test probe leads themselves, since the internal resistance of a device of this class is

negligible. Another measurement was made on a device for measuring the surface resistance. In this case, the measurement of the current from the voltage I(U) between the two probes is performed and the measurement of the voltage from the current U(I) between the other two probes. Both values should be linear so that the algorithm can handle the calculation of the resistance and conductivity values of the material. Attempts with different parameters and measurement locations failed because the I(U) relationship was exponential. The reason for this state of affairs may be ballistic, and not diffusion, charge transport in the metallic path resulting from nanometric channels between sintered CuZn alloy particles. The counterargument to this theory are the particles visible in the SEM images, the size of which exceeds 1 μm, and the radius of their sintering is significant (large sintering area between the particles). However, from the measurements carried out and the I(U) characteristic obtained in the four-probe mode, it can be approximated that the resistance of the material is less than 0.4 Ω, which indicates that it achieves the conductivity of pure metals.

4   Summary

In summary, this research investigated the deposition of metallic busbars using a high-pressure spraying process on various substrates for photovoltaic modules. The key findings and observations from this study include:

- Substrate variety: The study examined six different types of substrates for busbar deposition. These substrates included TCO glass, TCO glass with metallic copper (Cu) and titanium (Ti) coatings, and insulating alumina (III) (Al2O3) coatings prepared using physical vapor deposition and atomic layer deposition processes.

- Busbar thickness: The average thickness of the busbars was determined to be approximately 125±16 μm. There were slight variations in thickness between different substrates, with the smallest thickness of around 65 μm observed at the beginning of one of the busbars.

- Surface topography: The busbars exhibited rough surface topography at both micro- and nanometer scales. Despite this roughness, they displayed low resistivity, making them suitable for photovoltaic applications.

- Good adhesion: SEM images showed that the CuZn alloy of the bus-bars adhered well to the fluorine-doped tin oxide surface, as well as to fluorine-doped tin oxide surfaces covered with Cu, Ti or Al2O3 nanocoatings.

- Material reduction: The study demonstrated that it is possible to reduce the amount of copper (Cu) and silver (Ag) used in busbar production while maintaining low resistance values. This reduction in material usage can lead to cost savings in production.

- Versatile deposition technique: The presented high-pressure spraying process is effective for depositing conductive busbars on various surfaces, including glass, glass with a conductive layer (TCO), and polymer substrates. The relatively low deposition temperature allows for its use on different types of substrates, such as glass, TCO-coated glass, or silicon.

- Low resistance: The conductive busbars produced through this method exhibited low resistance, making them suitable for use in photovoltaic modules where efficient electrical conduction is essential.

Overall, the research suggests that the high-pressure spraying process is a promising technique for manufacturing cost-effective and efficient busbars for photovoltaic modules. It offers good adhesion, low resistance, and the potential for reducing material costs, which are all important factors for improving the performance and cost-effectiveness of solar energy generation.

Acknowledgments

References

[1] Bouraiou A., Hamouda M., Chaker A., Lachtar S., Neçaibia A., Boutasseta N., Mostefaoui M.: *Experimental evaluation of the performance and degradation of single crystalline silicon photovoltaic modules in the Saharan environment.* Energy **132**(2017), 22–30. doi: 10.1016/j.energy.2017.05.056

[2] Sharma V., Sastry O.S., Kumar A., Bora B., Chandel S.S.: *Degradation analysis of a-Si, (HIT) hetro-junction intrinsic thin layer silicon and m-C-Si solar photovoltaic technologies under outdoor conditions.* Energy **72**(2014), 536–546. doi: 10.1016/j.energy.2014.05.078

[3] Ding K., Chen X., Weng S., Liu Y., Zhang J., Li Y., Yang Z.: *Health status evaluation of photovoltaic array based on deep belief network and Hausdorff distance.* Energy **262**(2023), 125539. doi: 10.1016/j.energy.2022.125539

[4] Paggi M., Berardone I., Infuso A., Corrado M.: *Fatigue degradation and electric recovery in Silicon solar cells embedded in photovoltaic modules.* Sci. Rep. **4**(2014), 4506–4512. doi: 10.1038/srep04506

[5] Borri C., Gagliardi M., Paggi M.: *Fatigue crack growth in Silicon solar cells and hysteretic behaviour of busbars.* Sol. Energ. Mat. Sol. C **181**(2018), 21–29. doi: 10.1016/j.solmat.2018.02.016

[6] Infuso A., Corrado M., Paggi M.: *Image analysis of polycrystalline solar cells and modelling of intergranular and transgranular cracking.* J. Eur. Ceram. Soc. **34**(2014), 11, 2713–2722. doi: 10.1016/j.jeurceramsoc.2013.12.051

[7] Köntges M., Kunze I., Kajari-Schröder S., Breitenmoser X., Bjørneklett B.: *The risk of power loss in crystalline silicon based photovoltaic modules due to micro-cracks.* Sol. Energ. Mat. Sol. C **95**(2011), 4, 1131–1137. doi: 10.1016/j.solmat.2010.10.034

[8] Kaule F., Wang W., Schoenfelder S.: *Modeling and testing the mechanical strength of solar cells.* Sol. Energ. Mat. Sol. C **120**(2014), 441–447. doi: 10.1016/j.solmat.2013.06.048

[9] Taler J., Dzierwa P., Taler D., Harchut P.: *Optimization of the boiler start-up taking into account thermal stresses.* Energy **92**(2015), 160–170. doi: 10.1016/j.energy.2015.03.095

[10] Thomas M., Białecka B., Zdebik D.: *Removal of organic compounds from wastewater originating from the production of printed circuit boards by UV-Fenton method.* Arch. Env. Prot. **43**(2017), 4, 39–49. doi: 10.1515/aep-2017-0044

[11] Vogt T., Boden S., Andruszkiewicz A., Eckert K., Eckert S., Gerbeth G.: *Detection of gas entrainment into liquid metals.* Nucl. Eng. Des. **294**(2015), 16–23. doi: 10.1016/j.nucengdes.2015.07.072

[12] Braun S, Hahn G, Nissler R, Pönisch C, Habermann D.: *The multi-busbar design: an overview.* Energy Procedia **43**(2013), 86–92. doi: 10.1016/j.egypro.2013.11.092

[13] Schneider A., Rubin L., Rubin G.: *Solar cell efficiency improvement by new metallization techniques – the day4 electrode concept.* In: Proc. 2006 IEEE 4th World Conf. on C Photovoltaic Energy Conversion, Waikoloa, 2006, Vol. 1, 1095–1098. doi: 10.1109/WCPEC.2006.279333

[14] Braun S., Hahn G., Nissler R., Pönisch C., Habermann D.: *The Multi-busbar Design: An Overview.* Energy Proced. **43**(2013), 86–92. doi: 10.1016/j.egypro.2013.11.092

[15] Wang B., Jia X., Yang J., Wang Q.: *Numerical study on temperature rise and structure optimization for a three-phase gas insulated switchgear busbar chamber.* Energy **254**(2022), 124463. doi: 10.1016/j.energy.2022.124463

[16] Braun S., Hahn G., Nissler R., Pönisch C., Habermann D.: *Multi-busbar solar cells and modules: higher efficiencies and low silver consumptions.* Energy Proced. **38**(2013), 334–339. doi: 10.1016/j.egypro.2013.07.286

[17] Haverkamp H., Dastgheib-Shirazi A., Raabe B., Book F., Hahn G.: *Minimizing the electrical losses on the front side: development of a selective emitter process from a single diffusion.* In: Proc. 33rd IEEE Photovoltaics Specialist Conf. (PVSC), San Diego, 11-16 May 2008, **1**(2008), 4. doi: 10.1109/PVSC.2008.4922443

[18] Chen C., Pei X., Chen Y., Kang Y.: *Investigation, evaluation, and optimization of stray inductance in laminated busbar.* IEEE T. Power Electr. **29**(2014), 7, 3679–3693. doi: 10.1109/TPEL.2013.2282621

[19] Plesca A.: *Thermal analysis of busbars from a high current power supply system.* Energies **12**(2019), 2288. doi: 10.3390/en12122288

[20] Smirnova L., Juntunen R., Murashko K., Musikka T., Pyrhönen J.: *Thermal analysis of the laminated busbar system of a multilevel converter.* IEEE T. Power Electr. **31**(2016), 1479–1488. doi: 10.1109/TPEL.2015.2420593

[21] Varivodov V.N., Kovalev D.I., Zhulikov S.S., Golubev D.V., Romanov V.A., Mirzabekyan G.Z.: *Technological aspects of the use of cast polymer insulation for high-voltage switchgear and busbars.* Power Technol Eng. **54**(2021), 915–922. doi: 10.1007/s10749-021-01306-2

[22] Lu Y., Li G., Akhlaghi Y.G., Xuan Q., Pei G., Ji J., Zhao X.: *Effect of grid and optimization on improving the electrical performance of compound parabolic concentrator photovoltaic cells.* Sol. Energy **196**(2020), 607–615. doi: 10.1016/j.solener.2019.12.065

[23] Kyranaki N., Smith A., Yendall K., Hutt D.A., Whalley D.C., Gottschalg R., Betts T.R.: *Damp-heat induced degradation in photovoltaic modules manufactured with passivated emitter and rear contact solar cells.* Prog. Pchotovoltaics **30**(2022), 9, 1061–1071. doi: 10.1002/pip.3556

[24] Panda T., Sadhukhan S., Acharyya S., Banerjee P., Nandi A., Bose S., Mondal N., Das G., Maity S., Chaudhuri P., Saha H.: *Impact of multi-busbar front grid patterns on the performance of industrial type c-Si solar cel.* Sol. Energy **236**(2022), 790–801. doi: 10.1016/j.solener.2022.03.051

[25] Zhang Z., Zeng Y., Jiang C-S., Huang Y., Liao M., Tong H., Al-Jassim M., Gao P., Shou C., Zhou X., Yan B., Ye J.: *Carrier transport through the ultrathin silicon-oxide layer in tunnel oxide passivated contact (TOPCon) c-Si solar cells.* Sol. Energ. Mater. Sol. Cell. **187**(2018), 113–122. doi: 10.1016/j.solmat.2018.07.025

[26] Schneider A., Harney R., Aulehla S., Lemp E., Koch S.: *Progress in interconnection of busbar-less solar cells by means of conductive gluing.* Energy Proced. **38**(2013), 387–394. doi: 10.1016/j.egypro.2013.07.294

[27] Park J., Park N.: *Wet etching processes for recycling crystalline silicon solar cells from end-of-life photovoltaic modules.* RSC Adv. **4**(2014), 34823–34829. doi: 10.1039/C4RA03895A

[28] Zarmai M.Z., Ekere N.N., Oduoza C.F., Amalu E.H.: *A review of interconnection technologies for improved crystalline silicon solar cell photovoltaic module assembly.* Appl. Energ. **154**(2015), 173–182. doi: 10.1016/j.apenergy.2015.04.120

[29] Tyagi V.V., Rahim N.A.A., Rahim N.A., Selvaraj J.A.J.: *Progress in solar PV technology: Research and achievement.* Renew. Sustain. Energ. Rev. **20**(2013), 443–461. doi: 10.1016/j.rser.2012.09.028

[30] Jung T., Song H., Ahn H., Kang G.: *A mathematical model for cell-to-module conversio considering mismatching solar cells and the resistance of the interconnection ribbon.* Sol. Energy **103**(2014), 253–262. doi: 10.1016/j.solener.2014.01.032

[31] Oh W., Jee H., Bae J., Lee J.: *Busbar-free electrode patterns of crystalline silicon solar cells for high density shingled photovoltaic module.* Sol. Energ. Mater. Sol. Cell. **243**(2022), 11802. doi: 10.1016/j.solmat.2022.111802

[32] Oh W., Park J., Jeong C., Park J., Yi J., Lee J.: *Design of a solar cell electrode for a shingled photovoltaic module application.* Appl. Surf. Sci. **510**(2020), 145420. doi: 10.1016/j.apsusc.2020.145420

[33] Grätzel M.: *Dye-sensitized solar cells.* J. Photochem. Photobiol. C: Photochem. Rev. **4**(2003), 2, 145–153. doi: 10.1016/S1389-5567(03)00026-1

[34] O'Regan B., Grätzel M.: *A low-cost, high-efficiency solar cell based on dye-sensitized colloidal TiO_2 films.* Nature **353**(1991), 737–740. doi: 10.1038/353737a0

[35] Fortunato E., Ginley D., Hosono H., Paine D.C.: *Transparent conducting oxides for photovoltaics.* MRS Bull. **32**(2007), 3, 42–47. doi: 10.1557/mrs2007.29

[36] Noh S.I., Ahn H.-J., Riu D.-H.: *Photovoltaic property dependence of dye-sensitized solar cells on sheet resistance of FTO substrate deposited via spray pyrolysis.* Ceram. Int. **38**(2012), 5, 3735–3739. doi: 10.1016/j.ceramint.2012.01.018

[37] Kwak D.-J., Moon B.-H., Lee D.-K., Park C.-S., Sung Y.-M.: *Comparison of transparent conductive indium tin oxide, titanium-doped indium oxide, and fluorine-doped tin oxide films for dye-sensitized solar cell application.* J. Elec. Eng. Techn. **6**(2011) 5, 684–687. doi: 10.5370/JEET.2011.6.5.684

[38] Daghsen K., Lounissi D., Bouaziz N.: *A universal model for solar radiation exergy accounting: Case study of Tunisia.* Arch. Thermodyn. **43**(2022), 2, 97–118. doi: 10.24425/ather.2022.141980

[39] Singh J., Guo S., Peters I.M., Aberle A., Walsh T.: *Comparison of glass/glass and glass/backsheet PV modules using bifacial silicon solar cells.* IEEE J. Photovolt. **5**(2015), 99, 783–791. doi: 10.1109/JPHOTOV.2015.2405756

[40] Generowicz A., Gronba-Chyła A., Kulczycka J., Harazin P., Gaska K., Ciuła J., Ocłoń P.: *Life Cycle Assessment for the environmental impact assessment of a city' cleaning system. The case of Cracow (Poland).* J. Clean. Prod. **382**(2023), 135184. doi: 10.1016/j.jclepro.2022.135184

[41] Ciuła J., Kowalski S., Wiewiórska I.: *Pollution indicator of a megawatt hour produced in cogeneration – the efficiency of biogas purification process as an energy source for wastewater treatment plants.* J. Ecol. Eng. **24**(2023), 3, 232–245. doi: 10.12911/22998993/158562

[42] Deng S., Zhang Z., Ju C., Dong J., Xia Z., Yan X., Xu T., Xing G.: *Research on hot spot risk for high-efficiency solar module.* Energy Proced. **130**(2017), 77–86. doi: 10.1016/j.egypro.2017.09.399

[43] Kim K.A., Krein P.T.: *Photovoltaic hot spot analysis for cells with various reverse-bias characteristics through electrical and thermal simulation.* In: Proc. 2013 IEEE 14th Workshop on Control and Modeling for Power Electronics (COMPEL), Salt Lake City, 2013, 1–8. doi: 10.1109/COMPEL.2013.6626399

[44] Alwaeli M.: *Investigation of gamma radiation shielding and compressive strength properties of concrete containing scale and granulated lead-zinc slag wastes.* J. Clean. Prod. **166**(2017), 157–162. doi: 10.1016/j.jclepro.2017.07.203

[45] Solheim H.J., Fjær H.G., Srheim E.A., Foss S.E.: *Measurement and simulation of hot spots in solar cells.* Energy Proced. **38**(2013), 183–189. doi: 10.1016/j.egypro.2013.07.266

[46] Tomtas P., Skwiot A., Sobiecka E., Obraniak A., Ławińska K., Olejnik T.: *Bench tests and CFD simulations of liquid–gas phase separation modeling with simultaneous liquid transport and mechanical foam destruction.* Energies **14**(2021), 6, 1740. doi: 10.3390/en14061740

[47] Ocłoń P, Chin H.H, Kozak-Jagieła E., Taler J., Ścisłowicz F., Czamara M.: *33–Photovoltaic–Thermal Waste Heat Integration with Underground Thermal Energy Storage and Heat Pump Systems.* Handbook of Process Integration (2nd Edn.). Woodhead, 2023, 1017–1042. doi: 10.1016/B978-0-12-823850-9.00005-0

[48] Hadjidj M.S., Bibi-Triki N., Didi F.: *Analysis of the reliability of photovoltaic-microwind based hybrid power system with battery storage for optimized electricity generation at Tlemcen, north west Algeria.* Arch. Thermodyn. **40**(2019), 1, 161–185. doi: 10.24425/ather.2019.128296

[49] Hocine M., Abdessalam O.: *Simulation of photovoltaic panel cooling beneath a single nozzle based on a configurations framework.* Arch. Thermodyn. **42**(2021), 1, 115–128. doi: 10.24425/ather.2020.136950

[50] Thomas M., Białecka B., Zdebik D.: *Removal of organic compounds from wastewater originating from the production of printed circuit boards by UV-Fenton method.* Arch. Environ. Protect. **43**(2017), 4, 39–49. doi: 10.1515/aep-2017-0044

[51] Vogt T., Boden S., Andruszkiewicz A., Eckert K., Eckert S., Gerbeth G.: *Detection of gas entrainment into liquid metals.* Nucl. Eng. Des. **294**(2015), 16–23. doi: 10.1016/j.nucengdes.2015.07.072

[52] Bogdanowicz K.A., Augustowski D., Dziedzic J., Kwaśnicki P., Malej W., Iwan A.: *Preparation and characterization of novel polymer-based gel electrolyte for dye-sensitized solar cells based on poly(vinylidene fluoride-co-hexafluoropropylene) and poly(acrylonitrile-co-butadiene) or poly(dimethylsiloxane) bis(3-aminopropyl).* Copolymer. Mater. **13**(2020), 12, 2721. doi: 10.3390/ma13122721

[53] Abdulghafor I.A., Mnati M.J.: *Design of thermoelectric radiant cooling – photovoltaic panels system in the building.* Arch. Thermodyn. **43**(2022), 4, 85–108. doi: 10.24425/ather.2022.144407